Yeomans at the Jet Propulsion Laboratory, California Institute of Technology, for their helpful insights during the course of this work.

References

[1]Rayman, M. D., and Lehman, D. H., "NASA's First New Millennium Deep-Space Technology Validation Flight," International Academy of Astronautics, IAA Paper L-0502, April 1996.

[2]Williams, S. N., and Coverstone-Carroll, V., "Mars Missions Using Solar Electric Propulsion," *Journal of Spacecraft and Rockets*, Vol. 37, No. 1, 2000, pp. 71–77.

[3]Kluever, C. A., and Abu-Saymeh, M., "Mercury Mission Design Using Solar Electric Propulsion Spacecraft," *Journal of Spacecraft and Rockets*, Vol. 35, No. 3, 1998, pp. 411–413.

[4]Sauer, C. G., "Solar Electric Performance for Medlite and Delta Class Planetary Missions," American Astronautical Society, AAS Paper 97-726, Aug. 1997.

[5]Sims, J. A., "Trajectories to Comets Using Solar Electric Propulsion," American Astronautical Society, AAS Paper 00-134, Jan. 2000.

[6]Kluever, C. A., "Optimal Interplanetary Trajectories by Direct Method Techniques," *Journal of the Astronautical Sciences*, Vol. 45, No. 3, 1997, pp. 247–262.

[7]Pouliot, M. R., "CONOPT2: A Rapidly Convergent Constrained Trajectory Optimization Program for TRAJEX," Convair Div., General Dynamics, GDC-SP-82-008, San Diego, CA, Jan. 1982.

[8]Williams, S. N., "An Introduction to the Use of VARITOP: a General Purpose Low-Thrust Trajectory Optimization Program," Jet Propulsion Lab., California Inst. of Technology, JPL D-11475, Pasadena, CA, Jan. 1994.

[9]"Delta II Payload Planners Guide," Boeing Co. Space and Communications Group, MDC H3224D, Huntington Beach, CA, April 1996.

D. B. Spencer
Associate Editor

Numerical Heat Transfer Study over Spiked Blunt Bodies at Mach 6.8

R. C. Mehta*
Vikram Sarabhai Space Center, Trivandrum 695 022, India

Introduction

HIGH-SPEED vehicles are designed to withstand severe aerodynamic heating conditions. Such vehicles include hypervelocity projectiles, reentry payload modules, and hypersonic aircraft. Maximum heating and the consequent potential for material erosion are typical problems associated in the nose region of the blunt body. For flight velocities of 2–4 km/s, the nose region experiences high heating rates, and material ablation may contribute to unacceptable perturbations in the vehicle's aerodynamic characteristics and flight path. As an example of the severity of the heating, the stagnation temperature at sea level for a velocity of about 3.1 km/s, that is, about Mach 8.9, corresponds to the melting point of tungsten. Therefore, there exists a need to develop an active or passive technique to reduce the heating rates in the vicinity of the nosetip region of the vehicle. Heat flux can be reduced by attaching a forward facing spike on the blunt nose of the vehicle. The spike is also an effective way to reduce the aerodynamic drag due to the reduced dynamic pressure in the separated flow region.[1]

Several experimental studies have been conducted to examine the forebody flowfield of the spiked blunt body. Most of the experimental investigations conducted in the 1950s concentrated on issues related to high pressures and heating rates around such configurations and possible mechanisms to reduce them. Stadler and Nielsen[2] carried out experiments on a hemisphere–cylinder configuration at freestream Mach numbers of 1.5, 2.67, and 5.0, and a Reynolds number in the range of 0.16×10^6–0.85×10^6 based on the diameter of the cylinder. Their experiments indicated a reduction in surface pressure and, consequently, the drag, with the attachment of the forward facing spike. However, an increase in heat transfer rates due to the spike were shown in comparison with the clean configuration. The increase in heat-transfer rates were attributed to the separated turbulent boundary layer periodically impinging on the outer region of the boundary layer on the blunt nose. The experimental investigation of Bogdonoff and Vas[3] indicated an initial drop in pressure at the nose of the forebody with increased spike length up to an L/D ratio of 3 (where L is the spike length and D is cylinder diameter). Chapman[4] found theoretically that the heat transfer across the separated laminar boundary layer was reduced to about 56% of the level associated with the attached laminar boundary layer. Crawford[5] experimentally investigated the effect of the spike length on the nature of the flowfield, the surface pressure distribution, and the heat flux variation for a freestream Mach number of 6.8 and Reynolds number 0.12×10^6–1.5×10^6 based on the cylinder diameter. According to his experimental analysis, the drag and the heat flux were reduced when the spike was lengthened, but the drag was not influenced by the spike length when the latter exceeds the blunt-body diameter by roughly four times.

These experimental investigations provide insight into the characteristics of the separated region created by an adverse pressure gradient and shock/boundary-layer interaction over the blunt nose. Unsteadiness of the flow caused by the spike of the blunt body was examined by Maull[6] in 1960. It was found that the shock wave around the body oscillates when the nose has a plane shape. Wood[7] investigated experimentally the flowfield over the spiked cone and found that the shape and size of a region of separated flow is controlled primarily by the flow near the reattachment point. Fluctuating pressures in spiked-induced flow separation was observed experimentally by Guenther and Reding.[8]

The features of the supersonic flowfield can be delineated through these experimental investigations. It is characterized by a conical shock wave from the tip of the spike, a reattachment shock wave on the blunt body, and a separated flow region ahead of the blunt body. A schematic of the flowfield over the spiked blunt body is shown in Fig. 1a. This flowfield has also been numerically investigated and physical aspects of the flowfield have been described. Yamauchi et al.[9] have numerically investigated the flowfield around a spiked blunt body at freestream Mach numbers of 2.01, 4.15, and 6.80 for different ratios of L/D. The focus of their analysis was to investigate the mechanism of drag reduction and the flowfield pattern at different freestream Mach numbers and spike lengths. However, flowfields around a spiked blunt body include phenomena that have not been described previously. In the present work, fluid dynamics and heat transfer studies were performed for a freestream Mach number of 6.8 for different spike lengths and for a Reynolds number of 0.14×10^6 based on the diameter of the hemispherical cap.

Governing Equations and Numerical Method

The time-dependent axisymmetric compressible Navier–Stokes equations were written in integral form, and the system of equations was augmented by the ideal gas law for solution. The coefficient of molecular viscosity was calculated according to Sutherland's law. The flow was assumed to be laminar, which is consistent with the experimental study of Crawford[5] and the numerical simulation of Yamauchi et al.[9]

The flowfield code employs a finite volume discretization technique. The spatial and temporal terms are decoupled using the method of lines. The spatial computational domain was divided into a finite number of nonoverlapping quadrilateral cells. Thus, the discretized solution to the governing equations results in a set of volume-averaged state variables of mass, momentum, and energy, which are in balance with their area-averaged fluxes (inviscid and viscous) across the cell faces.[10] The finite volume code constructed in this manner reduces to a central difference scheme and is second-order accurate in space provided that the mesh is smooth enough. The cell-centered spatial discretization scheme is nondissipative; therefore, artificial dissipation terms are included as a blend of a Laplacian and biharmonic operator in a manner analogous to the second and fourth difference. The artificial dissipation term was added explicitly to prevent numerical oscillations near shock waves to

Received 8 February 2000; accepted for publication 5 May 2000.

*Engineer, Aerodynamics Division. Senior Member AIAA.

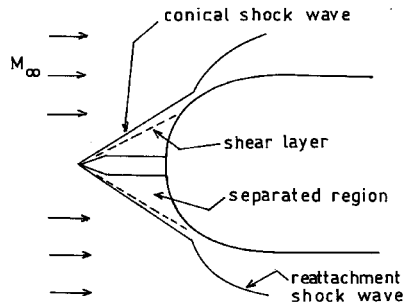

Fig. 1a Schematic of flowfield over spiked blunt body.

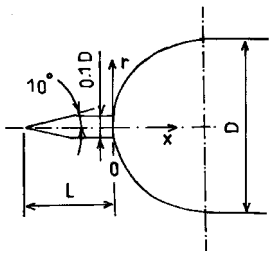

Fig. 1b Dimensions of the spiked blunt body.

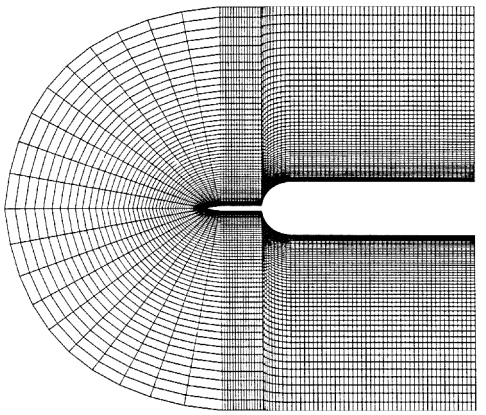

Fig. 1c Computational grid.

damp high-frequency undamped modes. Temporal integration was performed using the three-stage time-stepping scheme of Jameson et al.[11] based on the Runge–Kutta method. The artificial dissipation is evaluated only at the first stage. The details of this flowfield technique are further described in Ref. 12.

Conditions to corresponding to a freestream Mach number M_∞ of 6.8 are given as an initial condition. All variables were extrapolated at the outer boundary, and the no-slip wall condition was used to implement the boundary conditions. An isothermal wall condition was prescribed for the surface of the model, that is, a wall temperature of 300 K. The symmetry condition is applied on the centerline.

The dimensions of the spiked blunt body considered in the present analysis are shown in Fig. 1b and are the same as investigated by Crawford.[5] The model is axisymmetric, the main body has a hemisphere–cylinder nose, and diameter D is 7.62×10^{-2} m. The spike consists of a conical part and a cylindrical part. The angle of the spike's cone is 10 deg, and the diameter of the cylinder of the spike is $0.1D$. Spike lengths L of $0.5D$, $1.0D$, and $2.0D$ are considered in the present numerical analysis.

One of the controlling factors for the numerical simulation is the proper grid arrangement. The grid points are generated by a homotopy scheme.[13] Grid-independence tests were carried out, taking into consideration the effect of the computational domain, the stretching factor to control the grid intensity near the wall, and the number of grid points in the axial and normal directions. The outer boundary of the computational domain is varied from 5 to 12 times the cylinder diameter D. The grid stretching factor in the radial direction is varied from 1.5 to 5. The present numerical analysis was performed on 132×52 grid points. The outer boundary of the computational domain is maintained at 12 times the cylinder diameter. Figure 1c shows the grid used in the numerical computation. This grid arrangement is found to give a relative difference of about $\pm 1.5\%$ in the drag coefficient. The convergence criterion is based on the difference in density values, ρ, at any grid point between two successive iterations, that is, $|\rho^{n+1} - \rho^n| \leq 10^{-5}$, where n is the iteration index.

Results and Discussion

Figure 2 shows the computed flowfield for the spike lengths of $L/D = 0.5$, 1.0, and 2.0 at $M_\infty = 6.8$. In Fig. 2, interaction between the conical oblique shock wave starting from the tip of the spike and the reattachment shock wave of blunt body is observed. The reflected reattachment wave and shear layer from the interaction are shown behind the reattachment shock wave. A large separated region is observed in front of the blunt body and the shear layer; the

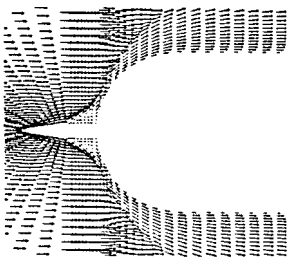

a) Velocity vector plot: $L/D = 0.5$

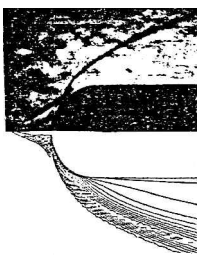

c) Schlieren picture and density contour plot: $L/D = 0.5$

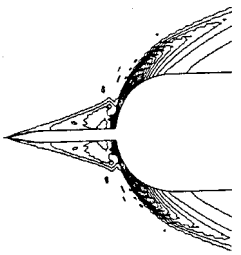

e) Pressure contour plot: $L/D = 1.0$

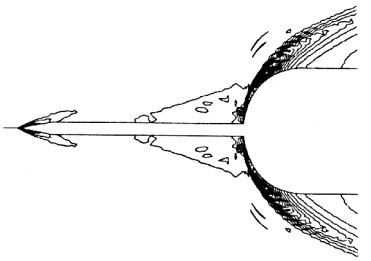

g) Pressure contour plot: $L/D = 2.0$

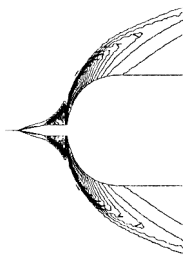

b) Pressure contour plot: $L/D = 0.5$

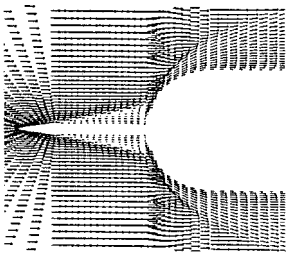

d) Velocity vector plot: $L/D = 1.0$

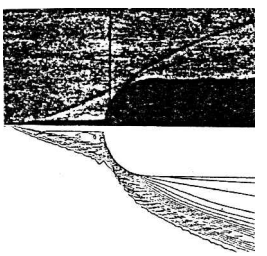

f) Schlieren picture and density contour plot: $L/D = 1.0$

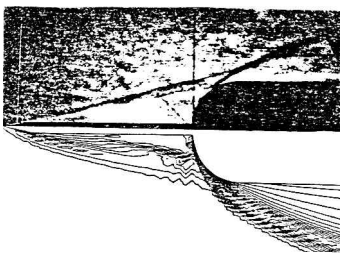

h) Schlieren picture and density contour plot: $L/D = 2.0$

Fig. 2 Flowfield for the spiked blunt body.

boundary of the separated region is clearly seen in Fig. 2. Similar flowfield features were obtained by Yamauchi et al.[9]

Computed density contour plots with schlieren photographs are also shown in Fig. 2 for different spike lengths. Flow patterns for $L/D = 1.0$ and 2.0 are similar to that of $L/D = 0.5$. However, when the spike length is large, the angle of the oblique shock wave from the spike tip decreases, and flow separation occurs slightly downstream. Because the reattachment point moves aft and the spike is relatively long, the length of the separated region extends. The angle of the conical shock wave depends on the angle of the shear layer, which gives an effective body shape to the outer freestream. The computed flowfields show agreement with the schlieren photographs taken in the experiment by Crawford.[5] According to these computed flowfields, the angle of the conical shock wave is much larger than that of a single cone of 10 deg. This difference may be attributed to the recirculating region acting as if it were a body boundary. This feature effectively causes the reduction in the drag.[1,9]

Figure 3 shows the nondimensional surface pressure variations along the spiked blunt body with L/D as a parameter. The wall pressure p is normalized by freestream pressure p_∞. The $x/R = 0$ location is the spike/nosetip junction as shown in Fig. 1b, where R is radius of the cylinder. The location of the maximum pressure on the surface of the spiked blunt body is at a body angle of about 40 deg for all L/D. This location corresponds to the reattachment point. A wavy pressure distribution is seen on the spike, which may be attributed to the present numerical algorithm. The maximum as well as the global pressure level decreases when L/D increases. There is some discrepancy between the numerical prediction and experimental data[5] in the vicinity of the reattachment point, but the shape of the distribution is the same as the experiment results. The maximum pressure becomes lower as the spike length is increased. The location of the maximum pressure point moves aft as the spike length increases.

Drag coefficient C_D vs the spike length are plotted in Fig. 4. The drag is reduced when the spike length increased. It can be seen in Fig. 3 that the pressure on the surface of the body with a longer spike is smaller. Because the pressure on the nose in the separated region is very low, the resulting drag becomes small. The flow around the spiked blunt body is similar to the flow around a single cone of more than 10 deg. As expected, the drag of the blunt body is remarkably influenced by the spike length. The maximum drag coefficient difference between the present result and the experimental data of

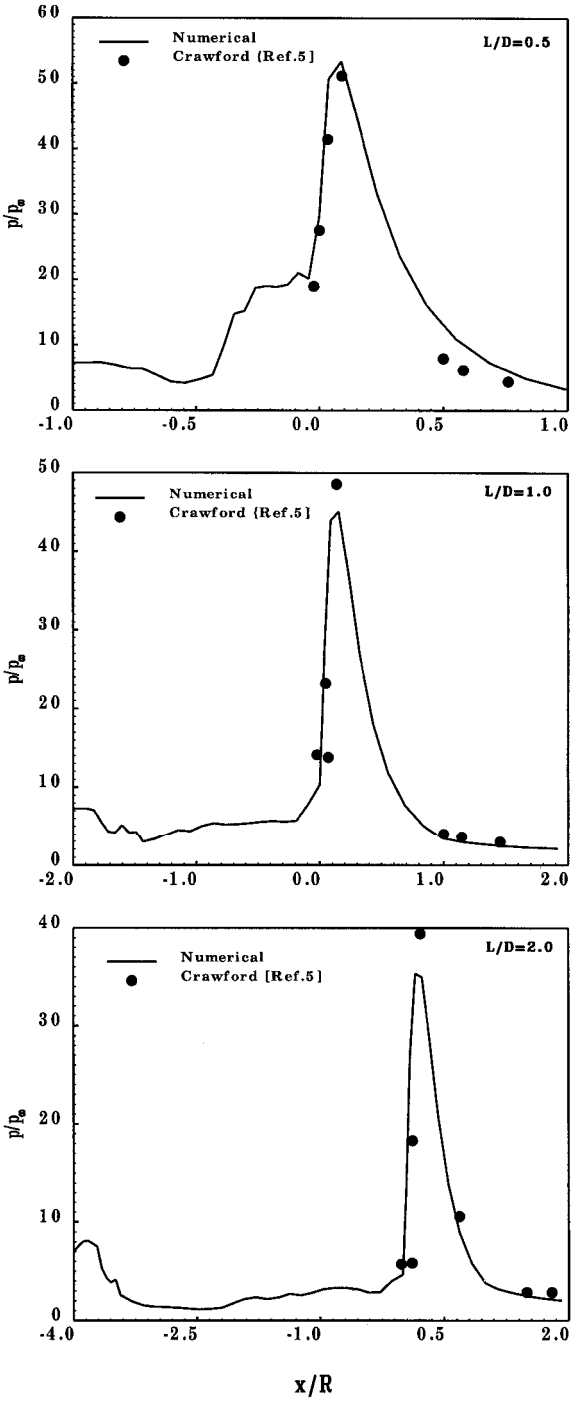

Fig. 3 Pressure distribution along the spiked blunt body.

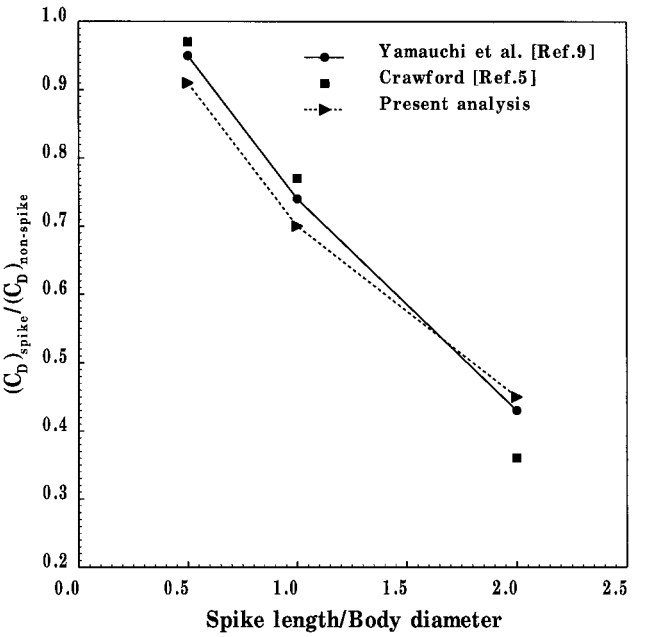

Fig. 4 Variation of drag coefficient.

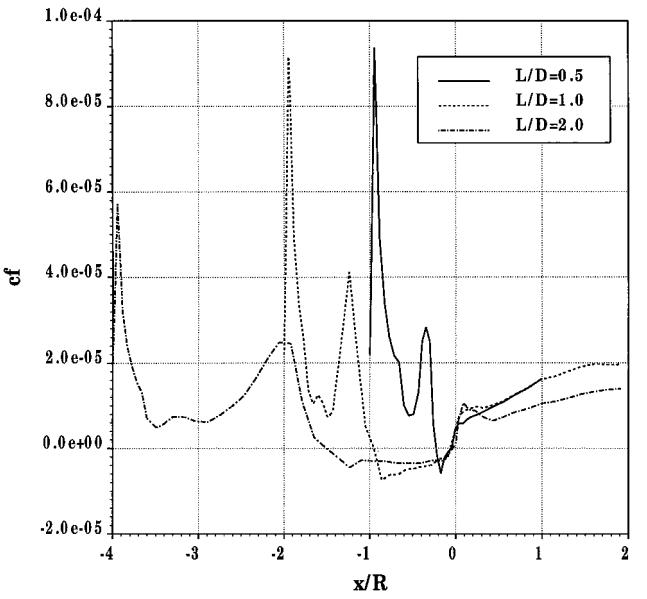

Fig. 5 Variation of surface skin-friction coefficient.

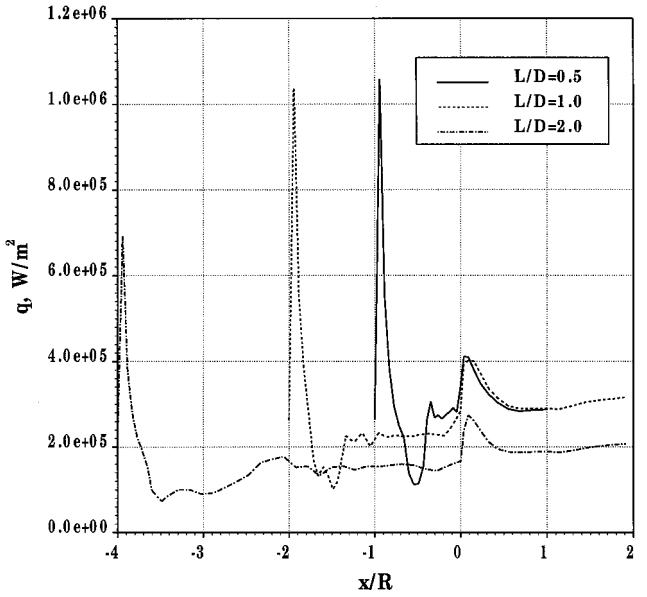

Fig. 6 Variation of wall heat flux.

Crawford[5] at $L/D = 2.0$ is found to be about 20%. The accuracy of the measured data is not available.

Figures 5 and 6 show the computed variation of surface skin-friction coefficient Cf and wall heat flux q along the spike blunt body. Negative skin friction can be seen on the spike, which is due to flow separation. The separation zone is found to be a function of the spike length. A sharp and sudden rise of skin friction and heat transfer is found very close to the spike tip, which is due to flow stagnation. The secondary peak heat flux is observed at about the reattachment point. This secondary peak heat flux decreases with increasing spike length.

Conclusions

The flowfield around a forward facing spike attached to a hemisphere–cylinder nosetip has been calculated at a freestream Mach number of 6.8 for different spike lengths. The flow features around the spiked blunt body are characterized by a conical shock wave emanating from the spike tip, a separated region in front of the blunt body, and the resulting reattachment shock wave for various freestream Mach numbers. The peak in local pressure and the heat flux are observed on the blunt-body region at the same position. The shear layer created by the spike passes through the reattachment shock wave giving the peak wall pressure and heat flux on the blunt body, which is influenced by the conical–shock reattachment interaction.

Acknowledgments

The author wishes to express his gratitude to the journal editors and reviewers for giving valuable suggestions toward the improvement of the present Note.

References

[1]Reding, J. P., Guenther, R. A., and Richter, B. J., "Unsteady Aerodynamic Considerations in the Design of a Drag-Reduction Spike," *Journal of Spacecraft and Rockets*, Vol. 14, No. 1, 1977, pp. 54–60.

[2]Stadler, J. R., and Nielsen, H. V., "Heat Transfer from a Hemisphere-Cylinder Equipped with Flow-Separation Spikes," NACA TN 3287, Sept. 1954.

[3]Bogdonoff, S. M., and Vas, I. E., "Preliminary Investigations of Spiked Bodies at Hypersonic Speeds," *Journal of the Aerospace Sciences*, Vol. 26, No. 2, 1959, pp. 65–74.

[4]Chapman, D. R., "A Theoretical Analysis of Heat Transfer in Region of Separated Flow," NACA TN 3792, June 1956.

[5]Crawford, D. H., "Investigation of the Flow over a Spiked-Nose Hemisphere Cylinder at a Mach Number of 6.8," NASA TN D-118, Dec. 1959.

[6]Maull, D. J., "Hypersonic Flow over Axially Symmetric Spiked Bodies," *Journal of Fluid Mechanics*, Vol. 8, Pt. 4, 1960, pp. 584–592.

[7]Wood, C. J., "Hypersonic Flow over Spiked Cones," *Journal of Fluid Mechanics*, Vol. 12, Pt. 4, 1962, pp. 614–627.

[8]Guenther, R. A., and Reding, J. P., "Fluctuating Pressure Environment of a Drag Reduction Spike," *Journal of Spacecraft and Rockets*, Vol. 14, No. 12, 1977, pp. 705–710.

[9]Yamauchi, M., Fujii, K., Tamura, Y., and Higashino, F., "Numerical Investigation of Supersonic Flows Around a Spiked Blunt Body," AIAA Paper 93-0887, Jan. 1993.

[10]Peyret, R., and Vivind, H., *Computational Methods for Fluid Flow*, Springer-Verlag, Berlin, 1993, pp. 109–111.

[11]Jameson, A., Schmidt, W., and Turkel, E., "Numerical Solution of Euler Equations by Finite Volume Methods Using Runge–Kutta Time Stepping Schemes," AIAA Paper 81-1259, June 1981.

[12]Mehta, R. C., "Numerical Investigation of Viscous Flow over a Hemisphere-Cylinder," *Acta Mechanica*, Vol. 128, No. 1–2, 1998, pp. 48–58.

[13]Shang, J. S., "Numerical Simulation of Wing-Fuselage Aerodynamic Interference," *AIAA Journal*, Vol. 22, No. 10, 1984, pp. 1345–1353.

M. Torres
Associate Editor

Boat Tail Effect of a Payload Fairing on the Elastic Displacement Response

V. Ramamurti*
Indian Institute of Technology, Chennai 600 036, India
and
S. Rajarajan† and G. V. Rao‡
Vikram Sarabhai Space Center, Trivandrum 695 022, India

Nomenclature

$[C]$	=	damping matrix
$[D_p]$, $[D_f]$	=	in-plane and bending stress–strain matrix
E	=	Young's modulus
$f(t)$	=	forcing function
h	=	thickness of the plate
$[K]$	=	assembled global stiffness matrix
$L1, L2, L3$	=	area coordinates
$[M]$	=	assembled global mass matrix
$\{u, v, w\}$	=	nodal displacements
α, β	=	constants
$\{\delta_p\}$, $\{\delta_f\}$	=	in-plane and bending nodal displacement vector
$\{\varepsilon\}$	=	total strain
$\{\varepsilon_p\}$, $\{\varepsilon_f\}$	=	in-plane and bending strain
$\{\theta_x, \theta_y, \theta_z\}$	=	nodal rotations of plate and shell element
υ	=	Poisson's ratio
ϕ, φ, θ	=	nodal rotations of beam elements
ω	=	natural frequency, rad/s

Introduction

THE main structural purpose of the payload fairing in any launch vehicle is to protect the payload from aerodynamic loading, heating, acoustic vibration, and other environmental conditions during the ascent phase and to provide an aerodynamic forward surface. The payload fairing is no longer required once the vehicle clears the atmosphere. Hence, it is jettisoned as soon as its purpose is served, to save weight and to allow for the separation of the satellite. A payload fairing is made in two or more sectors. The Atlas fairing is made in two 180-deg halves, and explosive bolts are used to begin separation. Spring-loaded actuators at the top of the cone section push the halves apart, while the aft end of each fairing half begins to rotate on hinges on a structure called the stub adaptor.[1] The Japanese H-ll rocket satellite fairing is also made in two halves, and

Received 8 November 1999; revision received 24 March 2000; accepted for publication 5 May 2000.

*Professor, Machine Dynamics Laboratory.
†Engineer, Launch Vehicle Design Group.
‡Group Director, Structural Engineering Group.